THE JOURNAL OF PHYSICAL CHEMISTRY Letters

Letter

Cite This: J. Phys. Chem. Lett. 2019, 10, 836−841

pubs.acs.org/JPCL

Self-Powered Dual-Color UV−Green Photodetectors Based on SnO_2 Millimeter Wire and Microwires/$CsPbBr_3$ Particle Heterojunctions

Yong Zhang, Wenxin Xu, Xiaojie Xu, Jian Cai, Wei Yang, and Xiaosheng Fang*

Department of Materials Science, Fudan University, Shanghai 200433, People's Republic of China

Supporting Information

ABSTRACT: Multiband detection has always been a challenge and has drawn much attention in the development of photodetectors (PDs). Herein, we present controllable synthesis of SnO_2 wires with different sizes via chemical vapor deposition and formed composites with $CsPbBr_3$ particles to realize dual spectral response. We constructed PDs based on a single SnO_2 millimeter wire decorated with $CsPbBr_3$ particles (SnO_2 MMW/$CsPbBr_3$), which showed a stepped spectrum, fast response speed, and self-powered function. Meanwhile, SnO_2 microwires/$CsPbBr_3$ composites (SnO_2 MWs/$CsPbBr_3$) were also utilized to fabricate PDs. It is noteworthy that detection occurred in two different wavelength bands (320 and 520 nm) with equivalent intensity at a bias of 0 V. The self-powered feature of this device comes from the built-in electric field at the interface of SnO_2/$CsPbBr_3$, and the dual-color response originates from asymmetric junction barriers between conduction bands of SnO_2 and $CsPbBr_3$. This work demonstrated promising self-powered PDs that are capable of multiband detection.

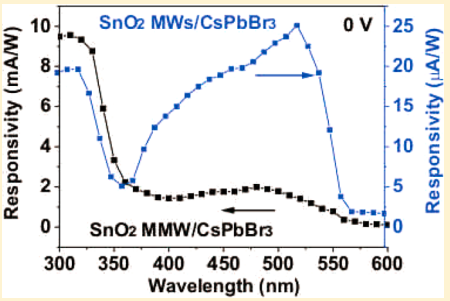

Photodetection technology is crucial for wide applications in versatile fields, such as remote control, flame detection, environmental monitoring, and communication.[1−8] With the increase of energy crisis worldwide, self-powered photodetectors (PDs) attract great attention by working without external driving forces as a built-in electric field contributes to its photocurrent response under zero bias. Recently, researchers have been developing self-powered PDs with better performance or integrated features.[9−13] Dual response is one of the promising features to expand its capacity. The detection range of various PDs covers almost all of the spectral segments. However, a single PD usually has a specific spectral response range. To satisfy some special requirements in applications with regard to full color imaging and so on,[14,15] investigations on PDs with dual wavelengths are particularly important.

Because of its stability and high electron mobility, tin oxide (SnO_2) has become an important material in the fields of optoelectronic devices. As an oxide semiconductor with a wide bandgap of ∼3.6 eV, SnO_2 is frequently used as an ultraviolet PD (UV PD). Various SnO_2 nanostructures such as single millimeter wires (MMWs), nanowire arrays,[16,17] nanonets,[18] and nanofibers[19] have been fabricated and tested for UV PDs. Among them, devices based on SnO_2 wires or arrays with materials like inorganic TiO_2[20] or organic PEDOT:PSS[21] are discovered with self-powered properties. However, few works have represented dual-wavelength response. Therefore, it is worthwhile to investigate the properties based on SnO_2 wire PDs.

All-inorganic perovskite $CsPbBr_3$ is a perovskite material attracting intensive interests.[22,23] It has been investigated for its remarkable optoelectronic properties because of the advantages of high electron mobility and small exciton binding energy.[24] Moreover, $CsPbBr_3$ has high stability, and its film can be integrated into various optoelectronic devices.[25,26] There have been reports on PbSe wires with a $CsPbBr_3$ shell that show good optoelectronic performance, including high responsivity (∼10^4 $A·W^{-1}$) and fair response speed (∼ms).[27] Despite the great physical and chemical properties and ease of composition, there are few studies focusing on the devices based on $CsPbBr_3$ and SnO_2 wires. Consequently, utilizing $CsPbBr_3$ to form composites with SnO_2 wires deserves consideration.

In this work, we investigated the photoelectric properties of SnO_2/$CsPbBr_3$ composites. SnO_2 microwires (MWs) and MMWs are obtained by chemical vapor deposition. To induce the growth of SnO_2 MWs, the substrates were sputtered with Au. Additional, MWs would elongate when the reaction time and temperature were further increased. Subsequently, $CsPbBr_3$ in solution was transferred onto the SnO_2 MWs and MMWs, and $CsPbBr_3$ would crystallize and form the SnO_2/$CsPbBr_3$ composites with further heat treatment. It is found that PDs based on single SnO_2 MMW/$CsPbBr_3$ composites have shown not only self-powered features but also stepped spectral responsivities. PDs based on SnO_2 MWs/$CsPbBr_3$ composites represent dual-wavelength response (320 and 520 nm) under zero voltage bias. Our work indicates that the different photoresponse based on different SnO_2/$CsPbBr_3$ composites is very promising for practical applications.

Figure 1a−c shows the X-ray diffraction (XRD) patterns of the SnO_2 MMW, SnO_2 MWs, and $CsPbBr_3$ particles,

Received: January 18, 2019
Accepted: February 6, 2019
Published: February 6, 2019

DOI: 10.1021/acs.jpclett.9b00154
J. Phys. Chem. Lett. 2019, 10, 836−841

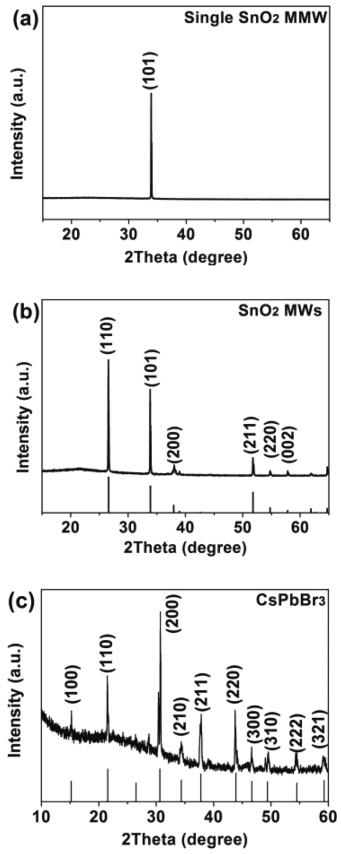

Figure 1. XRD patterns of (a) SnO_2 MMWs, (b) SnO_2 MWs, and (c) $CsPbBr_3$ particles.

respectively. The strong and sharp diffraction peak of the SnO_2 MMW at 33.9° corresponds to the (101) crystal face of rutile SnO_2 (Figure 1a). No other peaks are noticeable, suggesting that the as-obtained SnO_2 MMW possesses a single-crystal structure. All of the peak positions of pure SnO_2 MWs and their relative intensities are in good agreement with rutile SnO_2 with lattice parameters of $a = b = 4.738$ Å and $c = 3.187$ Å (JCPDF No. 41-1445), confirming the crystallinity and purity of the as-obtained sample (Figure 1b). The diffraction peaks for the pure SnO_2 MWs appearing at 26.6, 33.9, and 51.8° are attributed to (110), (101), and (211) crystal facets. The diffraction peaks of the $CsPbBr_3$ particles match well with the phase of $CsPbBr_3$ (JCPDF No. 54-0752) (Figure 1c). The sharp peak located at 30.6° is assigned to the (200) plane, and the diffraction peaks with 2θ of 15.2, 21.6, 37.8, and 43.9° are indexed to the (100), (110), (211), and (220) planes of the $CsPbBr_3$.

Furthermore, X-ray photoelectron spectroscopy (XPS) characterizations were performed to characterize the surface composition of the SnO_2 and $CsPbBr_3$. Figure S1a displays the total survey spectrum of the SnO_2 sample and reveals the dominant existence of elements Sn and O. As shown in Figure S1c, the splitting peaks of Sn 3d at 487.1 and 495.5 eV are related to Sn $3d_{5/2}$ and Sn $3d_{3/2}$, depicting the presence of Sn in the tetravalent oxidation state. Figure S1b displays the total survey spectrum of the $CsPbBr_3$ sample. As shown in Figure S1d, the binding energy peaks located at 739.3 and 725.3 eV can be ascribed to the spin orbital splitting photoelectrons of Cs $3d_{3/2}$ and Cs $3d_{5/2}$. The binding energy peaks located at 144.6 and 139.7 eV can be assigned to Pb $4f_{5/2}$ and Pb $4f_{7/2}$, confirming the existence of Pb^{2+} in $CsPbBr_3$ samples (Figure S1e). The binding energy peaks located at 70.0 eV can be assigned to Br $3d_{5/2}$, confirming the existence of Br in $CsPbBr_3$ samples (Figure S1f). Moreover, signals from other impurities cannot be detected in the SnO_2 and $CsPbBr_3$, proving the high purity of the as-prepared samples, which corresponds well with the results in XRD characterization.

Figure 2a,b shows a picture of the actual pictures of SnO_2 MMWs and SnO_2 MWs, which were grown by a typical

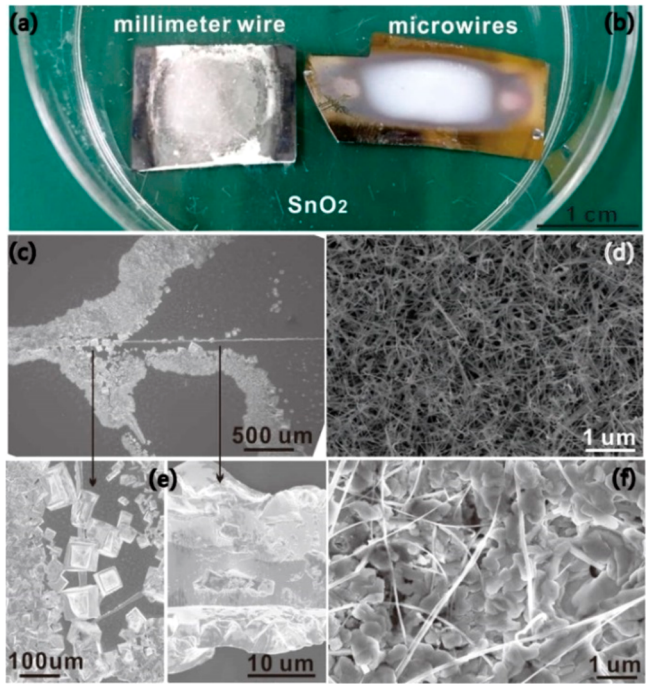

Figure 2. (a,b) Actual pictures of SnO_2 MMWs and SnO_2 MWs. SEM images: (c,e) SnO_2 MMW/$CsPbBr_3$ composites; (d) SnO_2 MWs; (f) SnO_2 MW/$CsPbBr_3$ composites.

chemical vapor deposition method. The SnO_2 MMWs with lengths of 2−6 mm were synthesized at 1300 °C, and the SnO_2 MWs were prepared at 1100 °C on a substrate that was presputtered with Au particles as the seed layer. The enlarged images of SnO_2 MWs in Figure 2d display that the pure SnO_2 MWs have diameters of about 10−100 nm and lengths of several microns, and the SnO_2 MWs are disorderly and interlaced together (Figure S2a). Figure 2c,e,f shows the scanning electron microscopy (SEM) images of the SnO_2 MMW/$CsPbBr_3$ and SnO_2 MW/$CsPbBr_3$ with different magnifications (Figure S2b). It is observed in Figure 2c that the SnO_2 MMW has a length over 3 mm. On the one side, the single MMW is embellished with a few $CsPbBr_3$ particles (the right image in Figure 2e), while on the other side, it is wrapped in $CsPbBr_3$ (the left image in Figure 2e). A single SnO_2 MMW was placed on a quartz substrate with a gentle slope in the long direction. The $CsPbBr_3$ solution was then dropped onto the higher right side and flowed to the left side due to the gravity force. With the evaporation of DMSO solvent and further heat treatment, $CsPbBr_3$ crystallized and was tightly bonded to the surface of the SnO_2 MMW. As in Figures 2f and S2b, the $CsPbBr_3$ particles are tightly attached to SnO_2 MWs that have different diameters and some lengths of more than 10 μm. The aspect ratio of SnO_2 in the composite can achieve more than 100, which shows the anisotropy of the products.

DOI: 10.1021/acs.jpclett.9b00154
J. Phys. Chem. Lett. 2019, 10, 836−841

To explore potentials of PDs based on single SnO_2 MMWs, we utilized $CsPbBr_3$, which is a research focus because of its unique physical and chemical properties to form composites with SnO_2 MMWs. Figure 3a demonstrates the structure of the

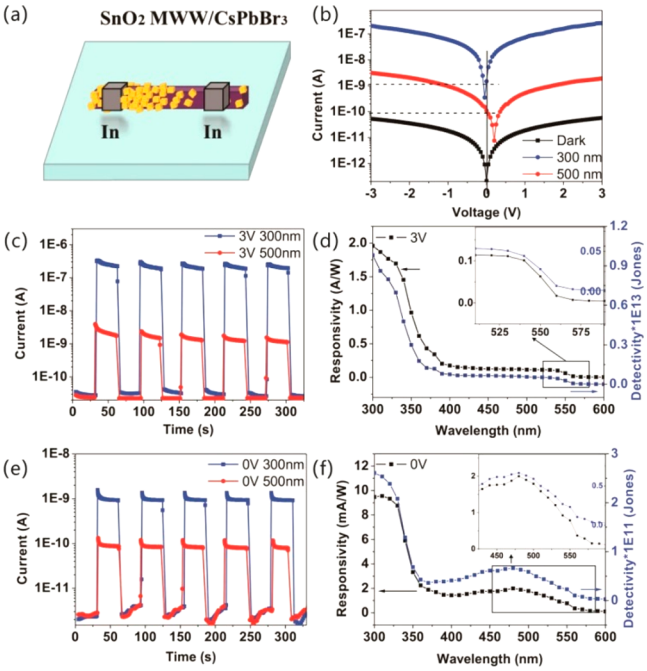

Figure 3. (a) Schematic diagram of the single SnO_2 MMW/$CsPbBr_3$. (b) $I-V$ curves of the SnO_2 MMW/$CsPbBr_3$ under dark and illumination of 300 and 500 nm. $I-t$ curves of the SnO_2 MMW/$CsPbBr_3$ with periodical on/off switching upon 300 and 500 nm light under biases of (c) 3 and (e) 0 V. Responsivities and detectivities of the SnO_2 MMW/$CsPbBr_3$ under the biases of (d) 3 and (f) 0 V.

PDs based on SnO_2 MMW/$CsPbBr_3$ composites. The typical current−voltage ($I-V$) curves of the SnO_2 MMW/$CsPbBr_3$ in a logarithmic plot are shown in Figure 3b in the dark and upon 300 and 500 nm light. SnO_2 MMW/$CsPbBr_3$ PDs show differences in the photocurrent and dark current, which means it obtains photoelectric properties. The photocurrents of the composites could reach 0.3 μA at biases of 3 V under illumination of 300 nm, around 5000 times as high as that in the dark. The photocurrent under 500 nm light was lower but still remained at a level of 3 nA. Noticeably, a relatively high photocurrent of 1 nA/0.1 nA under illumination of 300 nm/500 nm at nominal zero bias, as shown in Figure 3b, suggests that the hybrid device can operate without an external driving voltage. Figure S3a, showing the $I-V$ curves for pure SnO_2 MMWs in the dark and upon 300 nm light, indicate that the pure SnO_2 MMW device shows no self-powered properties. Therefore, it is concluded that the self-powered behavior in the SnO_2 MMW/$CsPbBr_3$ hybrid device is contributed from the built-in electric field between the SnO_2 MMW and $CsPbBr_3$.

Figure 3c exhibits the time-dependent current ($I-t$) curves of the SnO_2 MMW/$CsPbBr_3$ PD upon periodical 300 and 500 nm light at 3 V. Under light illumination of 300 nm at a bias of 3 V, the current rose to 0.3 μA and then declined to 30 pA with light on and off. This high photo-to-dark current ratio results partly from the good quality of SnO_2 with a single-crystalline structure, which can minimize the defect density, avoid the deleterious effects of defect and grain-boundary recombination, and facilitate the transport of carriers. By comparison, the current upon 500 nm was 2.5 nA/30 pA when the light was on/off. Figure S3b shows the $I-t$ curves of pure SnO_2 MMWs, which correspond well with Figure S3a. Under each cycle of switching on, the current instantly increases to 20 nA.

The spectral responsivity (R_λ) and detectivity are two other key parameters to evaluate the performance of a PD. The responsivity is defined as the photocurrent per unit of incident power, indicating how efficiently a detector responds to optical signals. It is usually calculated as below

$$R_\lambda = \frac{I_{ph} - I_d}{P_\lambda S} \tag{1}$$

where I_{ph} is the photocurrent, I_d is the dark current, P_λ is the light power density, and S is the effective area under irradiation. The detectivity (D^*, typically quoted in Jones), which reflects the ability to detect weak signals from the noise environment, is also a key merit for a PD. Considering that the major contributor of background noise is the shot noise from the dark current, the detectivity can be expressed as

$$D^* = \frac{R_\lambda}{(2eI_d/S)^{1/2}} \tag{2}$$

The detected spectral response ranges from 600 to 300 nm. The calculated results of SnO_2 MMW/$CsPbBr_3$ based PDs are shown in Figure 3d,f. Due to the high photocurrent and low dark current of the device, the maximum responsivity was 1.9 $A \cdot W^{-1}$, and the maximum value of D^* was 1.0×10^{13} Jones at 300 nm under 3 V. Such a high detectivity may be determined in a direct way.[28] The $I-t$ curves at zero bias (Figure 3e) showed a current of 1 nA/2 pA when the 300 nm light was on/off and 0.1 nA/2 pA when the 500 nm light was on/off. At zero bias, the responsivity was much lower compared with that at 3 V with a peak value of near 10 mA/W. It increased from 600 to 300 nm, which rose rapidly at a wavelength of about 320 nm with another sharp increase at around 520 nm (Figure 3f). The detectivity had a similar trend as that of the responsivity, with a maximum value of 2.6×10^{11} Jones. As shown in Figure S4, the rise time (t_r, the current to increase from 10 to 90%) and the decay time (t_d, the current to drop from 90 to 10%) of SnO_2 MMW/$CsPbBr_3$ composites are counted to be 0.03 and 1.94 ms at a bias of 0 V, which indicates an ultrafast response speed. The responsivity of pure SnO_2 MMW PDs under 3 V is shown in Figure S3c. A maximum responsivity of 0.38 $A \cdot W^{-1}$ was achieved at 300 nm, while it showed responsivities lower than 0.02 $A \cdot W^{-1}$ at 380 nm or longer wavelengths. The device is similar to a series circuit between SnO_2 and $CsPbBr_3$. Due to SnO_2 mainly contributing to the responsivity, the value of the photocurrent at a wavelength of 300 nm is much larger than that of 500 nm.

Other than MMWs, large quantities of SnO_2 MWs were also synthesized to further understand the properties of SnO_2/$CsPbBr_3$ PDs. $CsPbBr_3$ in DMSO solution was dropped onto the SnO_2 MWs and crystallized. The SnO_2 MW/$CsPbBr_3$ composite film (Figure 4a) was obtained after annealing at 70 °C for 30 min. Pure SnO_2 MW devices represent no self-powered behaviors, though they present photoelectric properties (Figure S5). Figure 4b indicates a typical optoelectronic performance SnO_2 MWs/$CsPbBr_3$ PD, which shows a self-powered property that originates from the heterojunction of SnO_2 MWs and $CsPbBr_3$ particles. The dark current remained less than 0.1 nA at 3 V, and the photocurrent under

DOI: 10.1021/acs.jpclett.9b00154
J. Phys. Chem. Lett. 2019, 10, 836−841

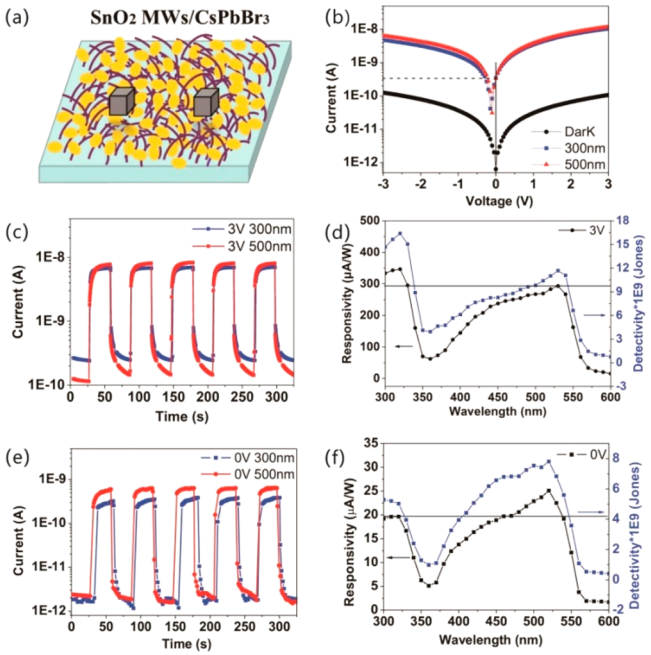

Figure 4. (a) Schematic diagram of the SnO_2 MW/$CsPbBr_3$; (b) $I-V$ characteristics of the SnO_2 MW/$CsPbBr_3$ under dark and illumination of 300 and 500 nm; $I-t$ curves of the SnO_2 MW/$CsPbBr_3$ with periodical on/off switching upon 300 and 500 nm light under biases of (c) 3 and (e) 0 V; responsivities and detectivities of the SnO_2 MW/$CsPbBr_3$ under biases of (d) 3 and (f) 0 V.

illumination of 300 and 500 nm of around 10 nA showed no apparent difference. When comparing the two groups of data displayed in Figure 4b, the currents under illumination of 300 and 500 nm are nearly the same when the light is on. Figure 4c–f represents the similarities and differences between the SnO_2 MW/$CsPbBr_3$ PD at 0 and 3 V. As depicted in Figure 4c, the current achieved 10 nA when light (300 and 500 nm) was switched on at 3 V. The dark current of 300 nm was 0.3 nA, larger than that under 500 nm light (0.1 nA). The $I-t$ curve displayed in Figure 4e shows that the photocurrent was around 0.6 and 0.4 nA under 500 and 300 nm light at 0 V, respectively. Once the light was switched off, the current decreased to less than 2 pA.

For pure SnO_2 MWs, the responsivity was close to 6 μA/W in the wavelength range of 350–600 nm but experienced a slight increase at shorter wavelength and reached a maximum value of 75 μA/W at a wavelength of 300 nm (Figure S5c). Notably, the SnO_2 MW/$CsPbBr_3$ hybrid device displays dual-color response. It possesses two peaks of responsivity that appear at 320 and 530 nm at 3 V (Figure 4d). With the increase of wavelength, the value of the responsivity rises slightly from 334 to 347 μA/W, followed by a considerable drop to the minimal value of 62 μA/W at 360 nm. Then it rises stepwise to the other peak value of 293 μA/W at 530 nm, which is a little less than the former peak value. Finally, it falls back to the lowest point. In Figure 4f, the spectral responsivity of the SnO_2 MW/$CsPbBr_3$ hybrid device at 0 V shares the same variation trend with that at 3 V. The spectral responsivity of the hybrid device at 0 V has local maximum value positions of 320 and 520 nm, and the peak values are 20 and 25 μA/W, respectively. When comparing the two groups of data sets in Figure 4d,f, although the SnO_2 MW/$CsPbBr_3$ PDs have similar local maximum value positions and peak values, and a difference in the relative responsivity upon 300 and 500 nm light illumination is observed. At a bias of 3 V, SnO_2 MWs have good photoelectric properties in the ultraviolet band. Consequently, the crest value is under light illumination of 320 nm. On the contrary, the built-in electric field of SnO_2 MW/$CsPbBr_3$ is the main factor that affects the responsivity at zero bias, and hence, the absolute maximum value is at 520 nm. As for the detectivities, the absolute values are 1.6×10^{10} and 1.2×10^{10} Jones under a bias of 3 V at wavelengths of 320 and 530 nm, respectively. At 0 V, the values are 5.2×10^{9} and 7.8×10^{9} Jones at wavelengths of 320 and 520 nm, respectively. This device can be considered as a parallel circuit between SnO_2 and $CsPbBr_3$; therefore, the intensity of the responsivities between the wavelength of 300 and 500 nm is almost equivalent.

As shown in Figure 5a,b, the reason for the dual-color response lies in the emergence of asymmetric junction barriers

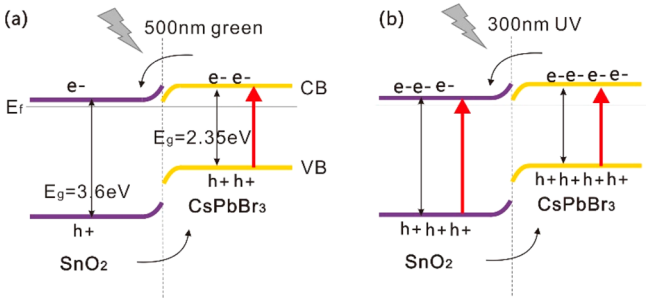

Figure 5. Schematic energy band diagrams of the SnO_2/$CsPbBr_3$ PD under light illumination of (a) 500 and (b) 300 nm showing the photogenerated carrier transfer process under light illumination.

between conduction bands of SnO_2 and $CsPbBr_3$. The asymmetric junction barriers cannot completely cut off the response of the visible light. The bandgaps of SnO_2 and $CsPbBr_3$ are 3.6 and 2.35 eV,[29,30] respectively. The absorption edge at around 520 nm resulted from the near-band-edge absorption of $CsPbBr_3$, and the absorption edge at around 320 nm originated from the near-band-edge absorption of SnO_2.[10] Under light illumination of 500 nm, $CsPbBr_3$ is excited, while SnO_2 is not. Driven by the built-in electric field, the electrons will flow to the conduction band of SnO_2 while the holes move toward the valence band of $CsPbBr_3$. The position of the conduction band in $CsPbBr_3$ is higher than that of SnO_2. However, the conduction band edge in $CsPbBr_3$ is lower than that of SnO_2, and a junction barrier is formed at the interface.[31] The existing junction barrier in the conductive band weakens the rectification effect of the heterojunction photodiode, resulting in a wavelength cutoff below the bandgap of SnO_2. When the incident wavelength lies between the two bandgaps, only $CsPbBr_3$ is photoexcited to generate photoinduced carriers, but the junction barrier drifts carriers back to $CsPbBr_3$ to keep electric neutrality, generating stable photocurrent below the photosensitive region of SnO_2. The SnO_2 MMW/$CsPbBr_3$ PDs show a stepped spectrum and self-powered properties, but the SnO_2 MW/$CsPbBr_3$ PDs show a self-powered dual-color with equivalent response intensity. Our study provides an alternative approach to fabricate PDs with dual response.

In summary, controllable synthesis of SnO_2 MMWs and SnO_2 MWs is realized by chemical vapor deposition. The SnO_2/$CsPbBr_3$ composites are then developed by dropping

DOI: 10.1021/acs.jpclett.9b00154
J. Phys. Chem. Lett. 2019, 10, 836–841

$CsPbBr_3$ solution onto SnO_2. For the SnO_2 MMW/$CsPbBr_3$ composite, the device shows a self-powered, fast response speed and stepped spectrum. For SnO_2 MW/$CsPbBr_3$, it exhibits a self-powered dual-color response (320 and 520 nm) with equivalent intensities. The built-in field between SnO_2 and $CsPbBr_3$ allows the device to operate without an external bias. The asymmetric junction barriers formed between conduction bands of SnO_2 and $CsPbBr_3$ result in the dual-color response. The results reported in this paper explore the dual-color self-powered PDs based on SnO_2 wires/$CsPbBr_3$ composites, providing a promising approach for future developments of high-performance multiband detected PDs.

EXPERIMENTAL METHODS

Preparation of SnO_2 MMWs. SnO_2 MMWs were prepared via a typical vapor transport process in a tube furnace. A mixture of SnO_2 and graphite with a weight ratio of 1:1 was loaded in a ceramic boat, where an equal amount of pure SnO_2 was loaded downstream. The previously cleaned Si/SiO_2 or quartz as the substrate was placed on the ceramic boat. Then the ceramic boat was put into a quartz tube. The temperature was increased to 1300 °C at a rate of 20 °C per minute, maintained for 90 min, and then declined naturally. A constant flow of nitrogen was used as the carrier and protecting gas in the entire process. A lot of SnO_2 MMWs were obtained on the substrate.

Preparation of SnO_2 MWs. SnO_2 MWs were obtained via a typical vapor transport route similar to the preparation of SnO_2 MMWs. The difference is that the substrate was sputtered with 20 nm Au particles as a seed layer in advance. The temperature was increased to 1100 °C at a rate of 20 °C per minute, maintained for 30 min, and then declined naturally. Large quantities of SnO_2 MWs were achieved on the substrate.

Fabrication of SnO_2/$CsPbBr_3$ Composites. To prepare the $CsPbBr_3$ solution, 0.4 M CsBr and 0.4 M $PbBr_2$ were dissolved in dimethyl sulfoxide (DMSO) solution. The solution was stirred and further filtered by using a syringe filter. SnO_2 MMWs and SnO_2 MWs were prepared as previously said. The $CsPbBr_3$ solution was then dropped onto the SnO_2-coated substrates and heated up to 70 °C for 30 min. Two small pieces of indium pastes were doctoral-bladed onto the composites as electrodes to construct PDs.

Characterization. The morphologies of the as-synthesized products were characterized by field emission SEM (FE-SEM Zeiss Sigma), XRD (Bruker D8-A25 diffractometer, Cu Kα radiation (λ = 1.5405 Å) in the 2θ range from 10 to 70°), and XPS (E PerkinElmer PHI 5000 C ESCA system equipped with a hemispherical electron energy analyzer). The binding energy for the C 1s peak at 284.6 eV was used as the reference for calibration. The photoelectric performances were characterized with a program-controlled semiconductor characterization system (Keithley 4200, U.S.A.). Time-resolved responses of the device were measured via the circuit, including with a Nd:YAG laser with a pulse duration of 3−5 ns (Continuum Electro-Optics, MINILITE II, 355 nm), an oscilloscope (Tektronix MSO/DPO5000), and a 1 GΩ resistor. The light intensity was measured with a NOVA II power meter (OPHIR Photonics). All of the measurements were performed in the ambient.

ASSOCIATED CONTENT

Supporting Information

The Supporting Information is available free of charge on the ACS Publications website at DOI: 10.1021/acs.jpclett.9b00154.

XPS, SEM, time-resolved response, $I-V$ curves, $I-t$ curves, and the responsivity of SnO_2 MMWs and SnO_2 MWs (PDF)

AUTHOR INFORMATION

Corresponding Author

*E-mail: xshfang@fudan.edu.cn.

ORCID

Xiaosheng Fang: 0000-0003-3387-4532

Notes

The authors declare no competing financial interest.

ACKNOWLEDGMENTS

This work was supported by the National Key Research and Development Program of China (2017YFA0204600), the National Postdoctoral Science Foundation of China (2017M621355), the National Natural Science Foundation of China (51721002, 11811530065, 51872050, and 11674061), and the Science and Technology Commission of Shanghai Municipality (18520710800, 17520742400, and 15520720700). Part of the experimental work was carried out in the Fudan Nanofabrication Laboratory.

REFERENCES

(1) Zhou, H.; Song, Z.; Grice, C. R.; Chen, C.; Yang, X.; Wang, H.; Yan, Y. Pressure-Assisted Annealing Strategy for High-Performance Self-Powered All-Inorganic Perovskite Microcrystal Photodetectors. *J. Phys. Chem. Lett.* **2018**, *9*, 4714−4719.

(2) Ouyang, W.; Teng, F.; Fang, X. S. High Performance BiOCl Nanosheets/TiO_2 Nanotube Arrays Heterojunction UV Photodetector: The Influences of Self-Induced Inner Electric Fields in the BiOCl Nanosheets. *Adv. Funct. Mater.* **2018**, *28*, 1707178.

(3) Zhan, Z.; Xu, L.; An, J.; Du, H.; Weng, Z.; Lu, W. Direct Catalyst-Free Chemical Vapor Deposition of ZnO Nanowire Array UV Photodetectors with Enhanced Photoresponse Speed. *Adv. Eng. Mater.* **2017**, *19*, 1700101.

(4) Zheng, L. X.; Hu, K.; Teng, F.; Fang, X. S. Novel UV-visible Photodetector in Photovoltaic Mode with Fast Response and Ultrahigh Photosensitivity Employing Se/TiO_2 Nanotubes Heterojunction. *Small* **2017**, *13*, 1602448.

(5) Yang, W.; Hu, K.; Weng, J. H.; Zhang, Y.; Fang, X. S.; Teng, F. High-performance Silicon-compatible Large-area UV-to-visible Broadband Photodetector based on Integrated Lattice-matched type II Se/n-Si Heterojunctions. *Nano Lett.* **2018**, *18*, 4697−4703.

(6) Chen, B. K.; Pradhan, N.; Zhong, H. Z. From Large-Scale Synthesis to Lighting Device Applications of Ternary I-III-VI Semiconductor Nanocrystals: Inspiring Greener Material Emitters. *J. Phys. Chem. Lett.* **2018**, *9*, 435−445.

(7) Xu, X.; Chen, J.; Cai, S.; Long, Z.; Zhang, Y.; Su, L.; He, S.; Peng, X. S.; Fang, X. S.; et al. A Real-Time Wearable UV-Radiation Monitor Based on a High-Performance P-CuZnS/N-TiO_2 Photodetector. *Adv. Mater.* **2018**, *30*, 1803165.

(8) Fang, X. S.; Hu, L. F.; Huo, K. F.; Gao, B.; Zhao, L. J.; Liao, M. Y.; Chu, P. K.; Bando, Y.; Golberg, D. New Ultraviolet Photodetector based on Individual Nb_2O_5 Nanobelts. *Adv. Funct. Mater.* **2011**, *21*, 3907−3915.

(9) Chen, Y. C.; Lu, Y. J.; Lin, C. N.; Tian, Y. Z.; Gao, C.; Dong, L.; Shan, C. X. Self-Powered Diamond/β-Ga_2O_3 Photodetectors for Solar-Blind Imaging. *J. Mater. Chem. C* **2018**, *6*, 5727−5732.

DOI: 10.1021/acs.jpclett.9b00154
J. Phys. Chem. Lett. 2019, 10, 836−841

(10) Ning, Y.; Zhang, Z. M.; Teng, F.; Fang, X. S. Novel Transparent and Self-powered UV Photodetector Based on Crossed ZnO Nanofiber Array Homojunction. *Small* **2018**, *14*, 1703754.
(11) Zhang, Z. M.; Ning, Y.; Fang, X. S. From Nanofibers to Ordered ZnO/NiO Heterojunction Arrays for Self-powered and Transparent UV Photodetectors. *J. Mater. Chem. C* **2019**, *7*, 223−229.
(12) Shahid, M.; Cheng, J.; Li, T.; Khan, M. A.; Wang, Y.; Hu, Y.; Zhang, M.; Yang, J.; Aziz, H. S.; Wan, C.; et al. High Photodetectivity of Low-Voltage Flexible Photodetectors Assembled with Hybrid Aligned Nanowire Arrays. *J. Mater. Chem. C* **2018**, *6*, 6510−6519.
(13) Yoo, J.; Jeong, S.; Kim, S.; Je, J. H. A Stretchable Nanowire UV−Vis−NIR Photodetector with High Performance. *Adv. Mater.* **2015**, *27*, 1712−1717.
(14) Ibrahem, M. A.; Verrelli, E.; Lai, K. T.; Kyriakou, G.; Lee, A. F.; Isaacs, M. A.; Cheng, F.; O'Neill, M. Dual Wavelength (Ultraviolet and Green) Photodetectors Using Solution Processed Zinc Oxide Nanoparticles. *ACS Appl. Mater. Interfaces* **2017**, *9*, 36971−36979.
(15) Hu, N.; Jiang, D.; Zhang, G.; Guo, Z.; Zhang, W.; Yang, X.; Gao, S.; Zheng, T.; Liang, Q.; Hou, J. Voltage Controlled Dual-Wavelength ZnO/Au/MgZnO UV Photodetectors. *Mater. Res. Bull.* **2018**, *103*, 294−298.
(16) Hu, L.; Yan, J.; Liao, M.; Wu, L.; Fang, X. S. Ultrahigh External Quantum Efficiency from Thin SnO_2 Nanowire Ultraviolet Photodetectors. *Small* **2011**, *7*, 1012−1017.
(17) Wu, J. M.; Kuo, C. H. Ultraviolet Photodetectors Made from SnO_2 Nanowires. *Thin Solid Films* **2009**, *517*, 3870−3873.
(18) Chen, H.; Hu, L.; Fang, X. S.; Wu, L. General Fabrication of Monolayer SnO_2 Nanonets for High-Performance Ultraviolet Photodetectors. *Adv. Funct. Mater.* **2012**, *22*, 1229−1235.
(19) Tian, W.; Zhai, T.; Zhang, C.; Li, S.; Wang, X.; Liu, F.; Liu, D.; Cai, X.; Tsukagoshi, K.; Golberg, D.; et al. Low-Cost Fully Transparent Ultraviolet Photodetectors Based on Electrospun ZnO-SnO_2 Heterojunction Nanofibers. *Adv. Mater.* **2013**, *25*, 4625−4630.
(20) Chen, D.; Wei, L.; Meng, L.; Wang, D.; Chen, Y.; Tian, Y.; Yan, S.; Mei, L.; Jiao, J. Visible-Blind Quasi-Solid-State UV Detector Based on SnO_2-TiO_2 Nanoheterostructure Arrays. *J. Alloys Compd.* **2018**, *751*, 56−61.
(21) Li, S.; Wang, S.; Liu, K.; Zhang, N.; Zhong, Z.; Long, H.; Fang, G. Self-Powered Blue-Sensitive Photodetector Based on PEDOT:PSS/SnO_2 Microwires Organic/Inorganic P−n Heterojunction. *Appl. Phys. A: Mater. Sci. Process.* **2015**, *119*, 1561−1566.
(22) Leung, S. F.; Ho, K. T.; Kung, P. K.; Hsiao, V. K. S.; Alshareef, H. N.; Wang, Z. L.; He, J. H. A Self-powered and Flexible Organometallic Halide Perovskite Photodetector with Very High Detectivity. *Adv. Mater.* **2018**, *30*, 1704611.
(23) Zhou, H.; Zeng, J.; Song, Z.; Grice, C. R.; Chen, C.; Song, Z.; Zhao, D.; Wang, H.; Yan, Y. Self-Powered All-Inorganic Perovskite Microcrystal Photodetectors with High Detectivity. *J. Phys. Chem. Lett.* **2018**, *9*, 2043−2048.
(24) Yantara, N.; Bhaumik, S.; Yan, F.; Sabba, D.; Dewi, H. A.; Mathews, N.; Boix, P. P.; Demir, H. V.; Mhaisalkar, S. Inorganic Halide Perovskites for Efficient Light-Emitting Diodes. *J. Phys. Chem. Lett.* **2015**, *6*, 4360−4364.
(25) Li, C.; Han, C.; Zhang, Y.; Zang, Z.; Wang, M.; Tang, X.; Du, J. Enhanced Photoresponse of Self-Powered Perovskite Photodetector Based on ZnO Nanoparticles Decorated CsPbBr3 Films. *Sol. Energy Mater. Sol. Cells* **2017**, *172*, 341−346.
(26) Protesescu, L.; Yakunin, S.; Bodnarchuk, M. I.; Krieg, F.; Caputo, R.; Hendon, C. H.; Yang, R. X.; Walsh, A.; Kovalenko, M. V. Nanocrystals of Cesium Lead Halide Perovskites (CsPbX3, X = Cl, Br, and I): Novel Optoelectronic Materials Showing Bright Emission with Wide Color Gamut. *Nano Lett.* **2015**, *15*, 3692−3696.
(27) Fan, C.; Xu, X.; Yang, K.; Jiang, F.; Wang, S.; Zhang, Q. Controllable Epitaxial Growth of Core−Shell PbSe@CsPbBr3 Wire Heterostructures. *Adv. Mater.* **2018**, *30*, 1804707.
(28) Fang, Y.; Armin, A.; Meredith, P.; Huang, J. Accurate Characterization of Next-Generation Thin-Film Photodetectors. *Nat. Photonics* **2019**, *13*, 1−4.
(29) Xue, M.; Zhou, H.; Ma, G.; Yang, L.; Song, Z.; Zhang, J.; Wang, H. Investigation of the Stability for Self-Powered $CsPbBr_3$ Perovskite Photodetector with an All-Inorganic Structure. *Sol. Energy Mater. Sol. Cells* **2018**, *187*, 69−75.
(30) Cai, J.; Xu, X.; Su, L.; Yang, W.; Chen, H.; Zhang, Y.; Fang, X. S. Self-Powered n-SnO_2/p-CuZnS Core−shell Microwire UV Photodetector with Optimized Performance. *Adv. Opt. Mater.* **2018**, *6*, 1800213.
(31) Wu, C.; Du, B.; Luo, W.; Liu, Y.; Li, T.; Wang, D.; Guo, X.; Ting, H.; Fang, Z.; Wang, S.; et al. Highly Efficient and Stable Self-Powered Ultraviolet and Deep-Blue Photodetector Based on $Cs_2AgBiBr_6$/SnO_2 Heterojunction. *Adv. Opt. Mater.* **2018**, *6*, 1800811.

DOI: 10.1021/acs.jpclett.9b00154
J. Phys. Chem. Lett. 2019, 10, 836−841